Defective graphene decorated with TiO$_2$ nanoparticles as negative electrode in Li-ion batteries

Michele Sidoli [a,b], Giacomo Magnani [a,b,*], Laura Fornasini [a,c], Silvio Scaravonati [a,b], Alberto Morenghi [a,b], Vincenzo Vezzoni [a,b], Danilo Bersani [c], Giovanni Bertoni [d,e], Mattia Gaboardi [f], Mauro Riccò [a,b], Daniele Pontiroli [a,b]

[a] Nanocarbon Laboratory, cIDEA & Department of Mathematical, Physical and Computer Sciences, University of Parma, Parco Area delle Scienze 7/A, 43124 Parma, Italy
[b] GISEL National Centre of Reference for Electrochemical Energy Storage Systems, INSTM National Interuniversity Consortium of Materials Science and Technology, Via Giusti 9, 50121 Firenze, Italy
[c] Department of Mathematical, Physical and Computer Sciences, University of Parma, Parco Area delle Scienze 7/A, 43124 Parma, Italy
[d] CNR – Istituto Nanoscienze, Via Campi 213/A, 41125 Modena, Italy
[e] IMEM – CNR, Institute of Materials for Electronics and Magnetism, Parco Area delle Scienze 37/A, 43124 Parma, Italy
[f] Elettra-Sinctrotrone Trieste S.C.p.A. Parco Area Science SS14, Km. 163.5, 34012 Basovizza, Italy

ARTICLE INFO

ABSTRACT

In this work, the performance of novel negative electrodes for Li-ion batteries based on defective graphene synthesized via a scalable thermal exfoliation of graphite oxide and decorated with TiO$_2$ nanoparticles is investigated. Titania polymorphs are interesting as battery electrode materials, owing to their high cycle stability, safety, abundance and negligible solid electrolyte interphase formation and volume changes upon cycling. Defective graphene, on the other hand, can embed TiO$_2$ nanoparticles, forming a conductive hybrid nanocomposite anode material for Li-ion batteries, with improved Li-ion and electron transport, optimising power density. Here we propose two different synthetic approaches for the decoration of graphene with TiO$_2$ nanoparticles: I) a novel chemical route where TiO$_2$ nanoparticles, mainly anatase, were grown on graphene in hydrothermal mild conditions and II) a physical solid-state approach where hydrothermal TiO$_2$ nanoparticles and graphene were mixed together via high energy ball-milling. The synthesized materials were analysed via powder X-ray diffraction, micro-Raman spectroscopy and HR-TEM, while the electrodes were electrochemically tested. Operando synchrotron diffraction was conducted on half-cell to investigate phase transitions in the electrode materials. Even in presence of small amount of graphene, significant improvement in capacity, reversibility, and high-rate capability were observed. In particular, the sample obtained through the addition of 1 wt% of graphene displayed a reversible capacity of more than 180 mA h/g after prolonged and wearing cycling. This result outperforms by 327 % the reversible capacity of pure TiO$_2$ electrode.

1. Introduction

Energy storage systems are facing a steady growth demand, due to the increased hunger for energy of the modern technological world. Among the strategies available today, rechargeable Li-ion batteries (LIBs) are the most versatile and considered the leading candidates for most of the applications [1]. The widening of LIBs employment and applications strongly depend on their safety, cost and environment impact. Most commercial batteries exploit critical materials which are either expensive, hard to substitute, or at risk of supply constraints (e.g. Co, Mn, Ni, etc.) [2]. Many materials have been developed recently, in order to enhance safety and performance of current commercial LIBs [3–6].

Lithium titanates, in particular Li$_4$Ti$_5$O$_{12}$ (LTO), represent a class of negative electrode materials already employed for commercial batteries, characterised by low environmental impact, high availability, reliability and safety [7], but with a relatively low specific charge capacity. This main limitation of LTO recently moved the scientific attention to TiO$_2$ as a possible candidate as an anode of LIBs. Among the most known polymorphs of TiO$_2$, the anatase and the bronze phases are considered the most electroactive, while rutile, being the most thermodynamically stable, is the least suitable

for electrochemical Li storage [8], unless the size of the particles is reduced to the order of nanometers [9]. Thanks to its lower molecular mass, TiO_2 would allow a larger specific charge capacity than LTO (up to 336 mA h/g theoretical, corresponding to the stoichiometry $LiTiO_2$), however keeping low-cost, long-life cycle and safe working voltage [10]. In fact, TiO_2 shows a relatively high Li insertion/extraction potential, which, on one hand, is responsible for the overall cell energy limitation, while, on the other hand, prevents Li plating on the anode, thus minimizing the formation of the Solid Electrolyte Interphase (SEI) [11]. As a drawback, TiO_2 large scale employment in LIBs is still hindered by the low Li ions mobility within the TiO_2 particles (from 10^{-15} to 10^{-9} cm^2 s^{-1}) and the poor electrical conductivity (10^{-12} S cm^{-1}) [12].

To overcome these limits, a plethora of solutions has been proposed so far. One approach consists in the tailoring of TiO_2 nanostructures, to maximize the electrical contact with the surrounding conducting agent. An array of possibilities opens, ranging from 0D TiO_2 to 1D, 2D, and 3D structures [13]. Another possible approach is the design of the conductive agent [14]. Studies show how the introduction of metals [15], metal oxides [16], and carbon materials [17–22] may improve the electrochemical performances of TiO_2. Still, most solutions offer great results, but show expensive drawbacks, employ toxic or carcinogenic materials (e.g. carbon nanotubes [17] or V_2O_5 [23]), or need difficult synthetic steps [24]. Compared to other conductive scaffolds, graphene appears to be the most promising one [25,26], providing high superficial area (up to 2630 m^2 g^{-1}), great electrical conductivity and structural flexibility, to accommodate the modest volume change associated with the TiO_2 lithiation [27,28], which decreases along with the nanoscale size of the particles [5]. For this reason, graphene has been widely employed in the LIB employing TiO_2 as an electroactive component: almost all of the research conducted in this field employs the decoration of graphene oxide (GO), using either sol-gel [29] or hydrothermal [30] syntheses. These synthetic pathways usually involve wet chemistry, hence solvent (water solutions [31,32], ethanol [33,34], etc.) needs to be removed to obtain the final product. High capacities above 180 mA h/g also at high C-rates have been reported for these systems [14].

In this work, two facile and scalable routes for the decoration of graphene by nanocrystalline TiO_2 particles were developed, and the hybrid nanocomposites have been studied as negative electrodes in LIBs. As a scaffold, a novel type of graphene obtained through a physical top-down approach was employed. This material was produced by thermal exfoliation of graphite oxide, synthesised via Brodie method, under dynamic vacuum; this allowed us to obtain a highly defective product. This graphene material, hereafter addressed as TEGO (Thermally Exfoliated Graphite Oxide), can be produced in large batches (gram scale) and is characterized by good physical properties [35–37]. By never exposing TEGO to air, active graphene defects, mainly in form of in-plane C vacancies and edges [38] proved to be beneficial for the decoration with metal and oxides nanoparticles [39], as they act as nucleation sites for further crystal growth [6]. Moreover, it has already been observed that TEGO can be employed as it is as a negative electrode both in LIBs and in Na-ion batteries [40]. Here, the decoration of TEGO was carried out following two different strategies: 1) by hydrolysis of a liquid titanium alkoxide (Ti-isopropoxide) via a green hydrothermal method, which is carried out in a autoclave reactor using only water as solvent. Different TEGO to TiO_2 ratios were tested and compared, and the role of graphene is discussed both in the synthetic step and in the electrochemical performances of the assembled device. 2) Alternatively, an all-solid-state method was also carried out to obtain the C/TiO_2 composite. For this synthesis, both TEGO and TiO_2 were mixed by means of energy ball milling, in order to obtain a composite. The choice of using these two methods is driven by the need of investigating green and fully scalable synthesis routes.

2. Experimental

2.1. Production of TiO_2 – TEGO materials

2.1.1. TEGO synthesis

The preparation of TEGO [41] followed a top-down approach starting with the oxidation of graphite (SGL Carbon, RW-A grade, 66 µm mean size). The oxidation was performed with the Brodie method [42], in which 5 g of graphite powder were ground with 40 g of sodium chlorate and kept at a temperature of about 2 °C with an ice bath. The powder was mechanically stirred, and 50 ml of fuming nitric acid (99+ %, Sigma Aldrich Co.) were added drop by drop. During this procedure it is important that the temperature of the slurry does not increase, and a strict control over the ice bath and the mixing speed is required. After the addition of the nitric acid, a thick slurry was obtained. The mixture was heated at 60 °C with a slow ramp and kept at that temperature for 8 h. After the reaction occurred, the slurry appeared dark greenish. The mixture was diluted in Milli-Q® water and filtered via fritted Büchner. The solid was then recovered and dispersed in a diluted (1 M) hydrochloric acid solution and filtered again, to remove the remaining salts. The solid was then suspended in Milli-Q® water, filtered and washed until the neutral pH of effluents turned neutral. The graphite oxide was then dried in an oven at 60 °C, mortared to powder and exfoliated in a tubular furnace at 1150 °C for 30 min under dynamic vacuum. This harsh step led to well exfoliated graphene platelets with an important presence of in-plane defects. The product was then recovered in an Ar glove box (MBraun Labmaster 130, O_2 and H_2O atmosphere below 0.1 ppm), without exposing it to air.

2.1.2. TiO_2 nanoparticles hydrothermal synthesis

This synthesis was performed to obtain a carbonless reference for the investigation. A solvothermal approach was chosen for the employment of relatively safe and inexpensive reagents, the facile execution, and the scalability of the process. TiO_2 nanoparticles were synthesised in a Teflon-lined stainless steel autoclave reactor, by hydrolysis of titanium (IV) isopropoxide (TTIP, 97 %, Sigma Aldrich Co.) [43], an organometallic precursor. Under inert Ar atmosphere, 3 ml of TTIP were inserted in a Pyrex glass vial which was then located inside the autoclave reactor. 5 ml of Milli-Q® water was poured inside the reactor, having care to avoid contact between the TTIP and water, to prevent uncontrolled hydrolysis of the precursor. The reactor was sealed and placed at 180 °C for 17 h. In these conditions the reaction reported in Eq. (1) took place:

$$Ti(OCH(CH_3)_2)_4 + 4H_2O \rightarrow TiO_2 + 4(CH_3)_2CHOH \tag{1}$$
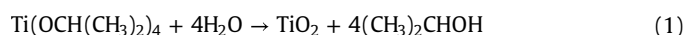
The reactor was cooled to room temperature, opened and the product was dried in a 60 °C oven overnight to evaporate the remaining water and isopropyl alcohol. The anatase product was mortared to achieve a fine powder. The final product was used as the blank sample, called Pure TiO_2.

2.1.3. TiO_2 nanoparticles decorated TEGO

This synthesis employed the same procedure used for the TiO_2 nanoparticles. In addition, TEGO was inserted inside the Pyrex® glass vial along with 3 ml of TTIP soaking the carbon host. For this synthesis, TEGO was always kept under Ar atmosphere and had no contact with air since its exfoliation, to avoid the oxidation of its defects [35,44]. As in the previous synthesis, Milli-Q® water was added in the cavity between the Pyrex® vial and the inner walls of the autoclave, without touching the C/Ti suspension. The reactor was sealed and underwent the same thermal treatment as the synthesis of pure TO_2 nanoparticles (180 °C for 17 h). The hydrolysis of the organotitanate takes place following the Eq. (1), but the presence of TEGO catalyses the crystallization in heterogeneous condition, thus decorating the carbon matrix. Two different relative concentrations

of TTIP and TEGO were tested to synthesize two different TiO$_2$:TEGO wt%, namely of 99:1 and 80:20. The final products will be hereafter called HT1 (99:1) and HT2 (80:20) respectively. The 99:1 ratio has been chosen according to our knowledge of how effective a small addition of graphene is in improving the composite properties [45] and by comparing our work with the state of the art [46]. The 80:20 ratio was chosen in order to probe a high carbon loading [47].

2.1.4. TEGO – TiO$_2$ nanoparticles mixed by ball milling (BM)

In order to compare the TiO$_2$-decorated TEGO prepared with our hydrothermal method to a sample prepared by simple mixing of the two components (Pure TiO$_2$ and TEGO), a solid-state mixing was performed. Both TEGO and hydrothermally synthesised TiO$_2$ were placed in an agate mortar jar along with 3 agate balls of a high energy vibratory ball mill (FRITSCH Mini-Mill PULVERISETTE 23). The reagents underwent 3 runs of 10 min each milling sessions at 30 Hz frequency, with a rest time of 5 min between the milling periods to avoid overheating and eventual side reactions. After the milling treatment, the powder was recovered from the bowl and the sample will be hereafter called BM. All samples investigated are listed in Table 1 reported below.

2.2. Electrodes fabrication and cell assembly

The active materials synthesized with the aforementioned processes were tested as electrodes in LIBs. Active materials were thoroughly ground in a mortar along with carbon black (CB, Timcal, Super 65) and polyvinylidene fluoride as a plastic binder (PVDF, Solvay, Solef® 6010). The ratio among the components was kept at 80 % active material, 10 % CB and 10 % PVDF. The powder mixture was transferred in a flat-bottomed flask and N-methyl-pyrrolidone (NMP, anhydrous 99.5 %, Sigma-Aldrich Co.) was added dropwise until a thick slurry was obtained. The product was mixed by magnetic stirring overnight and successively cast onto aluminum foil with a notch bar (0.3 mm thick). The wet cast was dried in a 60 °C oven for a couple of hours, then transferred in a 70 °C vacuum oven and left overnight under dynamic vacuum. The dried film was successively put under a hydraulic press at about 7 MPa, then punched in 12 mm diameter electrodes and further dried in a 70 °C vacuum oven. The dried electrodes were then moved inside the Ar-filled glovebox. The electrochemical devices were realised in a standard 2032 coin-cell case with a metallic lithium disc as the counter electrode. The electrolyte was prepared by dissolving lithium hexafluorophosphate 1 M (LiPF$_6$, ≥99.99 %, battery grade, Sigma Aldrich Co.) in an ethyl carbonate (EC, battery grade, Sigma Aldrich Co.) and dimethyl carbonate (DMC, battery grade, Sigma Aldrich Co.) 1:1 v/v solution. A Celgard® disc was employed as a separator. To produce the synchrotron-compatible cases, coin cells were properly modified to allow the passage of synchrotron light. In detail, a 7 mm diameter hole was drilled in the cell case and the current collector to keep an empty path for the synchrotron beam, operating in transmission configuration. 25 μm thick Kapton® windows were glued to the battery case to keep the cell airtight whilst minimizing beam absorption. The internal architecture was not modified.

Table 1
List of samples studied in the current work.

Sample	Synthesis method	TiO$_2$/TEGO (wt%)	Short ID
TiO$_2$	Hydrothermal	100	Pure TiO$_2$
TiO$_2$ decorated TEGO	Hydrothermal	99/1	HT1
TiO$_2$ decorated TEGO	Hydrothermal	80/20	HT2
TiO$_2$ / TEGO ball milled	Ball-milling	99/1	BM

2.3. Material characterization

2.3.1. Powder x-ray diffraction

Powder X-ray diffraction (PXRD) was performed in a Debye-Scherrer geometry with a Bruker D8 Discover diffractometer. The X-ray source employed was a copper anode (CuK$_\alpha$) coupled with a Göbel mirror and a 0.5 mm collimator, whereas a Rayonix MX225 2D area detector (with 73.2 μm pixels size) was used to collect the diffraction rings. Proper calibration of the detector was performed using a corundum standard. Images were processed with the software FIT2D and the extracted powder patterns were analysed using the GSAS-II suite. All samples were sealed into glass capillaries of 0.5 diameter and spun during the data collection. PXRD is a powerful method to quantitatively evaluate the amount of the different TiO$_2$ polymorphs and their relative ratio, and to extimate the average mean particle size of the crystalline fraction.

2.3.2. Raman spectroscopy

Micro-Raman measurements were performed with a Horiba Jobin Yvon LabRam (HORIBA Scientific, Kyoto, Japan) confocal microspectrometer (300 mm focal length), equipped with an Olympus BX40 microscope (Olympus, Tokyo, Japan), using a 50x ULWD objective, an 1800 groves/mm grating, a XY motorized stage and a Peltier cooled silicon CCD. The 473.1 nm line of a doubled Nd:YAG laser was used as excitation, with a spectral resolution of ∼4.0 cm^{-1}. The spectra were acquired in the spectral range from 100 to 2000 cm^{-1}. The system was calibrated using the 520.6 cm^{-1} Raman peak of silicon. To avoid heating effects on the samples, the laser excitation power was lowered by means of density filters. Typical acquisition times were 60 s repeated at least 10 times. Data analysis was performed with the LabSpec 5 software. Raman spectroscopy was employed to investigate the presence of the different TiO$_2$ polymorphs, even the amorphous fraction, and to study the disorder degree of graphene material.

2.3.3. Transmission electron microscopy

TEM analysis was performed via a field emission JEM-2200FS high-resolution microscope (JEOL Ltd. Japan). The electron source was a Schottky gun with an accelerating voltage of 200 kV, with a point resolution of 0.19 nm. Signal was cleared through an in-column "omega-type" energy filter before reaching the detectors (STEM detectors, high resolution CCD camera and an EDS detector). To perform the TEM investigation, the as-synthesised powders were dispersed in isopropanol. Few drops of the suspension were dropped onto a holey carbon film supported on a copper grid and the sample was then placed in the microscope. TEM was employed to determine the morphology of the different samples at the nanoscale, also highlighting the features of the TiO$_2$ nanoparticles supported on graphene.

2.3.4. Galvanostatic charge - discharge

The electrochemical measurements of the half-cells were performed in order to determine which composite material was the best performing as a negative electrode in a half Li-ion cell. The measurements were carried out with a Landt CT2001A battery testing system. The galvanostatic charge/discharge measurements (GCD) were performed at different C-rates, keeping the voltage window between 2.5 and 1 V [48].

2.3.5. Synchrotron diffraction

Operando synchrotron powder X-ray diffraction (SPXRD) in transmission geometry was performed on suitably modified coin-cells as discussed in the Section 2.2 on the MCX beamline at the Elettra synchrotron light source in Trieste (Italy) [49]. Powder patterns were collected at 12 keV (λ = 1.0332 Å) using a MAR-CCD165 area detector (80 μm pixels size), after suitable calibration using a

LaB$_6$ standard (SRM660a from NIST [50]) with 10 s per acquisition separated by 5 min breaks. Data reduction and integration of the 2D patterns were carried out using the GSAS-II suite [51]. For each sample, the 2D patterns for the entire run of cycling were merged together to detect spurious features repeating over time, which were then masked effectively prior integration. A minority of extra features randomly occurring during the operando experiment were easily spotted and removed. Integrated patterns were analysed by means of sequential Rietveld refinement starting using the known phases of pure and lithiated TiO$_2$. The low profile-resolution posed by this particular geometry is well compensated by the high resolution in time, obtained using a fast 2D detector. To gather additional information on the most interesting samples, pristine powders, composing the active materials of the batteries, were measured also on MCX at 12 keV in Debye-Scherrer geometry on the 4-circle Huber goniometer equipped with a high count-rate scintillator detector and receiving slits open at 0.2 mm (vertical) and 0.3 mm (horizontal). Borosilicate capillaries (0.3 mm diameter) were filled with powders and measured at room temperature while spinning at 300 rpm. The two known phases of anatase and brookite were Rietveld refined against the data using GSAS-II. A silicon standard (640c by NIST [52]) was used for establishing the instrumental profile for both 1D and 2D detectors in both geometries. SPXRD allowed us to follow the structure evolution of the crystalline TiO$_2$ electroactive fraction during the electrode operation.

3. Results and discussion

3.1. Powder x-ray diffraction

A sample consisting of pure hydrothermal titanium dioxide nanoparticles (Pure TiO$_2$) was synthesized and tested along with two stoichiometries of TiO$_2$ decorated TEGO (HT1 and HT2) to understand the optimal ratio between TiO$_2$ and carbon. PXRD indicated that Pure TiO$_2$ consists in a mixture of anatase and brookite (Fig. 1). The mean crystal size, calculated from the broadening of the diffraction peaks using the Scherrer equation through Rietveld refinement, results in an average 15–20 nm size. Rietveld method was also employed for the quantitative phase analysis. Anatase and brookite phase fractions were calculated being 82.7(4) % and 17.3(3) %
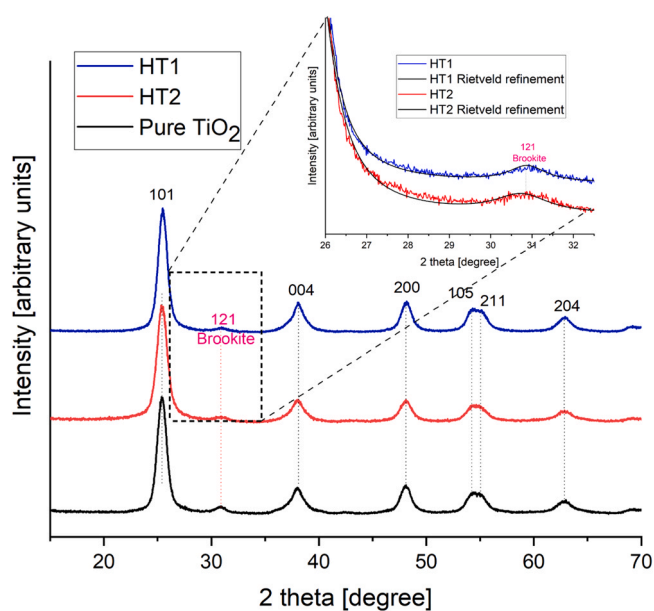
respectively. In the HT2 sample, the ratio between anatase and brookite turn out to be similar, being 82.1(4) % and 17.9(6) % in weight respectively. In HT1 sample, the ratio between the two polymorphs showed some differences, since it was found that the weight fraction of anatase was 88.3(3) %, and the brookite fraction was 11.7(3) %, thus suggesting a selective effect of the heterogeneous growth by graphene scaffold, favouring the anatase polymorph. The crystallite size estimation, performed with Scherrer estimation for HT1 gives 9.1(5) nm in size for anatase and 7.0(7) for brookite crystallites; HT2 showed similar results, measuring and 11.5(5) nm for anatase and 7.3(4) for brookite respectively. The observed crystallite size in the different samples correlates with the relative percentage of the anatase polymorphs, as anatase is known to be the most stable arrangement when the crystalline size is low [53].

The data are summarized in Table 2.

No rutile was observed in any of the sample, since the temperatures reached in the synthesis are not sufficiently high to promote the formation of the rutile polymorph. The heterogeneous growth of TiO$_2$ upon the carbon scaffold yielded smaller crystallites (as already observed in analogous systems [41]) and the low dimension of the particles is known being related to a favoured anatase structure with respect to the brookite phase [41]. For these reasons, HT samples were characterized by a smaller crystallite size and, as a consequence, a selection towards the anatase phase.

3.2. Transmission electron microscopy

These findings were confirmed by HRTEM characterization, which was conducted on the aforementioned samples. In Fig. 2a and b, Pure TiO$_2$ is shown at different magnifications. A spread distribution of the crystal sizes can be noted in the sample. The morphology of the crystallites shows the typical anatase features, i.e. truncated bipyramid shape (quasi octahedral, almost barrel-like). In some crystals the morphology appears different, and an almost spherical shape is observable. Also, in the case of HT samples (Fig. 2c and d), HRTEM analysis confirms the Scherrer-derived crystal size of TiO$_2$ NPs and gives a clearer insight on the morphology of the sample. It immediately appears that the mean size is lower than in the BL sample, and also in this case both truncated bipyramids and quasi-spherical crystals coexist. In the high-magnification image, the typical 0.35 nm interplanar distance of the (101) periodicity can be visualized. In addition, when twisted at the right angle, the cross section of TEGO can be observed. It appears as wrinkly layers crossing the sample, but at higher resolution, the stacking of graphitic planes can be clearly seen. For this reason, in TEM analysis it is hard to detect single layered TEGO. Finally, HRTEM analysis was performed on BM sample (2e and 2f). As aforementioned, no significative crystallinity was observable in the BM diffraction and this is confirmed by the TEM image, where the ordered and well-shaped bipyramid anatase nanocrystals observed in the previously investigated samples are no more noticeable, and an almost amorphous cluster of TiO$_2$ NPs is observed. Apparently, high-energy ball milling tends to agglomerate TiO$_2$ nanoparticles and to amorphize the crystallites. In BM images, it is hard to see the periodicity of crystal planes, and the surface of the particles appears jagged, probably as a consequence for the highly energetic the milling process. As a collateral result, TEGO does not appear as a sheet widely spread onto which TiO$_2$ NPs are tightly bound, but the milling process causes its folding in a nest-like structure onto which the NPs are surrounded. It is possible to identify and quantify the carbon content at the edges of these superstructures, and its morphology appears more amorphous than pristine TEGO.

Fig. 1. PXRD patterns of the samples, from bottom to top: Pure hydrothermal TiO$_2$, HT2 and HT1. It can be noticed that the brookite peak (at 2θ ∼ 31°) becomes less pronounced in the carbon scaffolded syntheses.

Table 2
PXRD data analysis of crystalline TiO_2-based samples.

Sample	Anatase wt%	Brookite wt%	Anatase mean size (nm)	Brookite mean size (nm)	R_{wp} %
Pure TiO_2	82.7(4)	17.3(3)	19.9(2)	15.0(6)	8.4
HT1	88.3(3)	11.7(3)	9.1(5)	7.0(7)	10.0
HT2	82.1(4)	17.9(6)	11.5(5)	7.3(4)	12.8
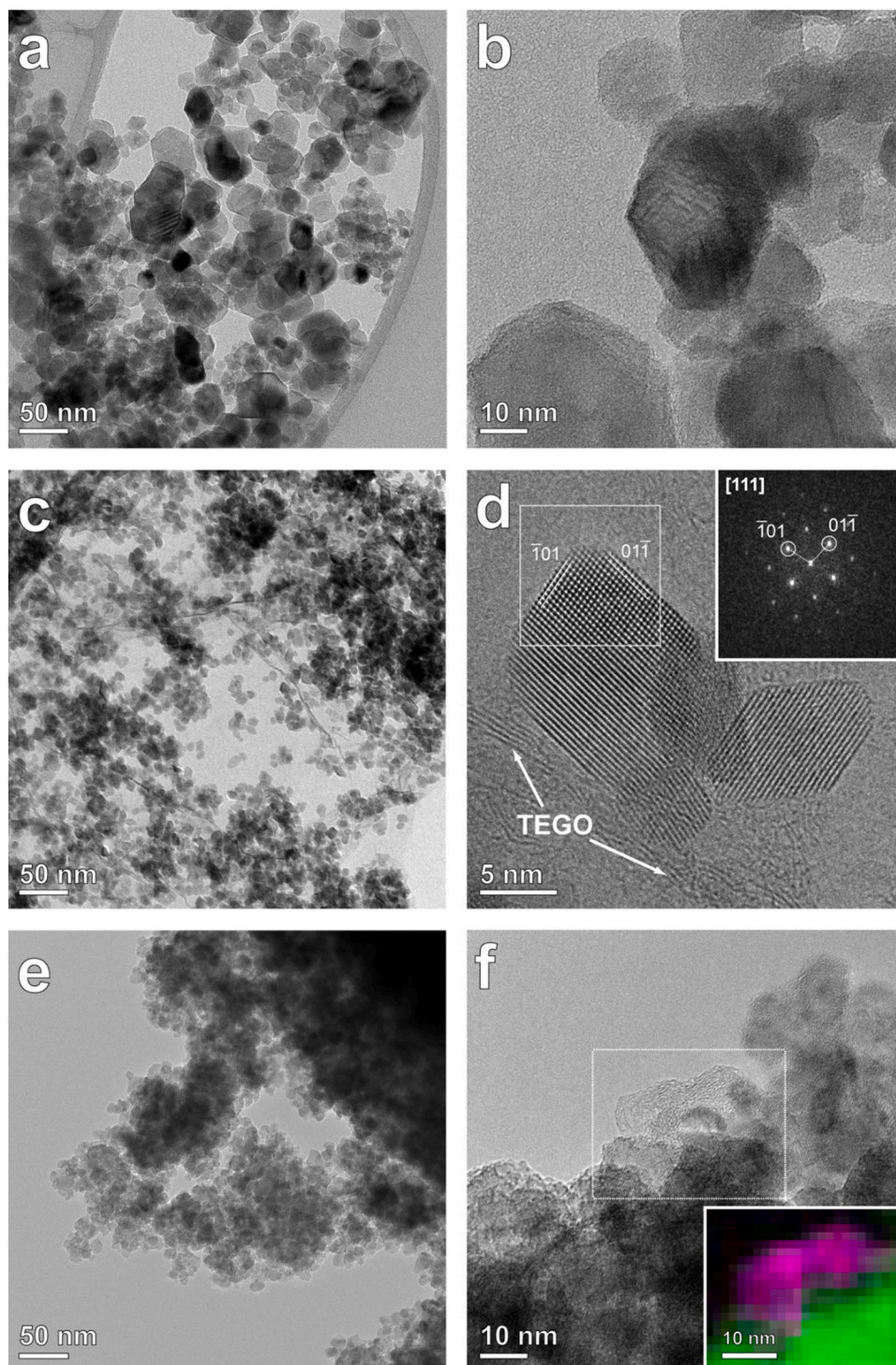
Fig. 2. HRTEM images titania and its graphene composites. a) Pure TiO_2. b) A higher magnification of the morphology of the bipyramidal shape of the titania crystal. c) a wide area of HT1. d) higher magnification of HT1. The characteristic form of the particle is shown and some multilayered TEGO can be noticed in the cross section. e) Low magnification of BM. The shape of the crystallites is less regular than in the previous samples. f) A detail of BM, where both titania and carbon are depicted. The insert depicts a colour compositional map, where pink is C and green is Ti.
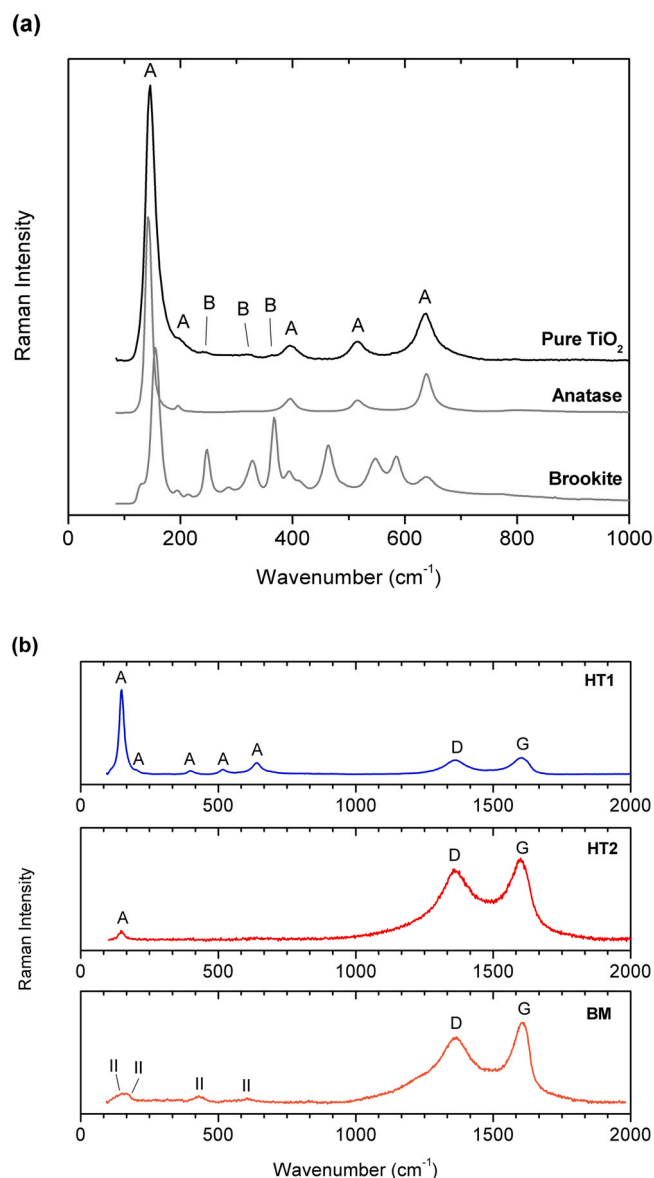
(a)

(b)

Fig. 3. (a) Raman spectra on Pure TiO₂ and reference spectra of crystalline anatase and brookite; (b) Raman spectra on HT1, HT2 and BM samples. TiO₂ features are marked: anatase (A), brookite (B), TiO₂-II (II). Graphene features are marked as D and G bands.

3.3. Micro-Raman spectroscopy

The nanostructure of TiO2 nanoparticles combined with TEGO was also proved by micro-Raman spectroscopy. Raman spectra on the HT and Pure TiO₂ samples are shown in Fig. 3. Crystalline anatase and brookite spectra are reported as reference in Fig. 3a. As well as observed with the PXRD analysis, the Pure TiO₂ sample consists mainly of anatase nanocrystals, together with a minor contribution of brookite (Fig. 3a). The five Raman peaks of the anatase structure were found at ~147, 198, 397, 516 and 637 cm^{-1}, whereas weaker signals corresponding to brookite features were detected at ~243, 320, 355 cm^{-1} [41]. The strongest peak of anatase, occurring at 147 cm^{-1} with a linewidth (FWHM) of 22 cm^{-1}, is shifted and broadened compared to that of crystalline anatase (peak position at 143 cm^{-1}, FWHM 14 cm^{-1}). This behavior is typical of nanoparticles smaller than 15–20 nm [54,55]: according to the phonon confinement model, the anatase Raman peaks broaden and shift following their phonon dispersion curve. Conversely, a sharp peak is observed

in crystalline anatase, at the frequency typical of the Γ point of the Brillouin zone. In both HT1 and HT2, TiO₂ was identified mainly as nanocrystalline anatase, as shown in Fig. 3b. In HT1, the anatase main peaks have been found at ~148, 200, 395, 517 and 640 cm^{-1}, whereas the brookite features are hardly visible. In HT2, only the strongest peak of anatase has been detected. Similar to the Pure TiO₂ material, the shift and broadening of the strongest anatase peak are assigned to the nanometric crystal size. On the contrary, in BM (Fig. 3b), TiO₂-II has been obtained after the ball-milling treatment, which is a titania polymorph with almost non-existing literature about its employment in LIBs. Broad bands occurring at ~145, 170, 425 and 605 cm^{-1} were observed, corresponding to the high-pressure phase, as expected from a high-energy ball-milling treatment [56]. In the high wavenumber spectral range in Fig. 3b, graphene signals are detected with the D and G bands, peculiar of carbon-based materials. The two broad bands occur at ~1360 cm^{-1} and ~1600 cm^{-1}, respectively. As the D band arises from disorder effects or defects in the imperfect crystalline structure, the defective structure of TEGO is further confirmed by the presence of the broad D band [57].

3.4. Electrochemical characterization

Electrochemical performances were tested via GCD analysis, within a potential window ranging from 2.5 to 1 volt vs Li/Li⁺. This range was chosen because of the well-known mechanism of discharge-charge process of a TiO₂-based lithium battery. During the discharge process, the Li⁺ ions intercalate inside the TiO₂ crystal lattice, resulting in a phase shift of the anodic material to an orthorhombic phase of lithium titanate. In this reaction, titanium reduces from Ti⁴⁺, reaching Ti³⁺ when 1 mol of lithium is fully intercalated in the crystal structure, following Eq. (2).

$$TiO_2 + xLi^+ + xe^- \leftrightarrow Li_xTiO_2 \tag{2}$$

Practically, the maximum Li insertion in the titania crystal lattice is hampered to the Li$_{0.5}$TiO₂ stoichiometry, due to strict thermodynamic restraints [58], resulting in an orthorhombic lithium titanate structure. Given the theoretical capacity of 335 mA h/g, the halved stoichiometry can grant 168 mA h/g, which is the capacity upon which the C-rate was calculated. Tests were conducted at different C rates to evaluate the performances under different conditions. Due to the chosen voltage window, only TiO₂ weight fraction was considered as the active material of the cell due to the limited capacity of TEGO (and carbon-based materials in general) in the selected voltage window [40,59–61]. Charge-discharge cycles were performed with a rest time of 30 min between both processes. This allowed to investigate the unbiased open circuit voltage after either the charge or the discharge, as the system is in a non-equilibrium state at the end of a charge or discharge semicycle, due to the finite lithium diffusion time from the front to the back of the electrode. From the capacity vs cycles plot (Fig. 4), a comparison between the different HT stoichiometries and the pure TiO₂ sample can be made. Pristine Pure TiO₂ shows no stabilization of the reversible capacity within the first cycles. At C/5 rate, a large specific discharge capacity of 184 mA h/g is achieved, but still a sudden capacity drop happens after few cycles, decreasing by 50 % at the 10th cycle. The reason of this notable loss of reversibility is the inability of the system to perform a full lithiation and delithiation even at slow rates, due to the insulating nature of the active material. With the addition of a moderate amount (1 %) of TEGO -HT1- this effect is successfully buffered, leading to a capacity fading of just 8 % within 10 cycles. In the sample HT2, a new phenomenon is observed. A noticeable value of 297 mA h/g first discharge capacity is registered, lowering at about 150 mA h/g after the first few cycles. This can be caused by the considerable TEGO fraction, which starts to show its own redox mechanisms and SEI formation at about 1.5 volt. As reported
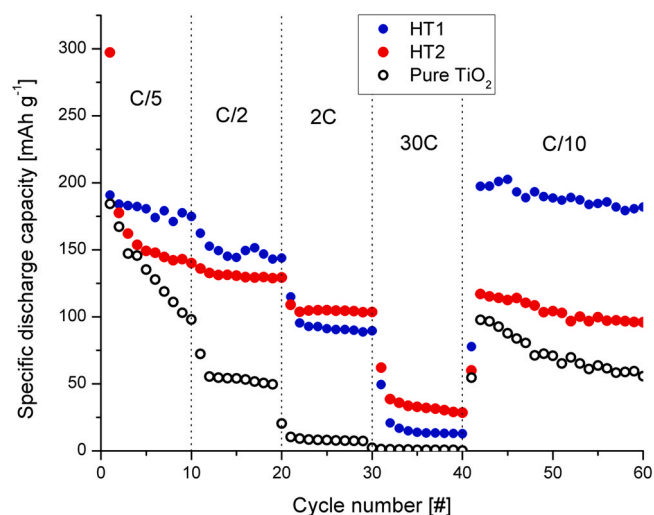
Fig. 4. GCD cycles of different samples are reported. Namely, different rates (from C/10–30 C) are shown.

elsewhere, TEGO has a high surface area (600 m^2/g) and displays a huge first cycle capacity [40] that reduces almost ten times during the subsequent cycles. This is caused by a massive SEI formation that employs a lot of energy to develop through all the surface of the material, leading to a high irreversible capacity that stabilizes within the first couple cycles of the device. In HT2 this effect is highlighted by the relevant TEGO content of the electrode.

At higher C rates, Pure TiO$_2$ shows poor performances due to the low electrical conductivity of the system, despite the important (10 %) addition of carbon black in the preparation of the slurry. Anatase nanoparticles polarize immediately under the high currents (up to 5 A/g) leading to a close to zero lithiation capacity. In HT1 at 2 C rates, the reversible capacity reaches up to 90 mA h/g, while depletes under 20 mA h/g at 30 C; this improvement in capacity is attributed to the effect that TEGO operates both during the synthetic step and during the cycling of the device. HT2 on the other hand, despite showing modest performances compared to the 99:1 stoichiometry at low C rates, proves its benefits at high C rates. The considerable amount of TEGO surrounding the anatase nanoparticles improves the high rate cyclability of the system allowing a reversible capacity above 30 mA h/g at 30 C, meaning about 20 % of the theoretical capacity in less than two minutes of charge time.

The increased capacity at high rates in TiO$_2$-TEGO electrodes could be rationalized as follow: on the one hand, the electrical conductivity of TEGO allows high-rate charge-discharge processes preventing polarization effects; on the other hand, anatase decorated TEGO displays a smaller size of the crystallites, allowing a more rapid and efficient lithium exchange at high rates. As it is known, these high-rate processes mostly operate via rapid mechanism on the surface of TiO$_2$ nanocrystals, meaning that smaller particles may lead to better high-rate storage. In fact, the charge-discharge mechanism can be divided into three regions (as shown in Fig. 5) [62], namely a first, monotonic steady stage in which voltage drops rapidly due to the onset of the lithium insertion/extraction, in a quasi-solid solution mechanism. In this stage, the smaller crystallites of TiO$_2$ help obtaining improved performances, since the lithium ions have a lower path to fully intercalate the particles. During the second stage, a long flat plateau corresponds to the crystal phase transition of the lithium titanate. Then, no more lithium can be

reversibly intercalated in the TiO$_2$ structure, however further storage can occur at the particle interfaces, leading to a third stage of lithium exchange, also favored by the crystallite size and the fast charge extraction provided by the carbon support. This third stage is also characterized by a steep decrease of the potential, since no phase transition occur [62]. Since the HT1 was proven as the best overall sample, except for high current density charges and discharges, in which the HT2 stoichiometry provided better results, a different synthetic approach was tested maintaining the same TiO$_2$:TEGO ratio. BM sample was produced with a 99:1 wt ratio. The electrode and the half-cell were then assembled in the same fashion of the other samples. This sample was synthesized and tested to better understand the role of TEGO. It was proven that the addition of TEGO in the synthesis step allowed the formation of smaller TiO$_2$ particles, but to better understand the enhancement in the electrochemical properties of the TiO$_2$-TEGO composite was produced by milling Pure TiO$_2$ and a tiny amount of TEGO, to confirm the crucial role of the impregnation of the matrix by the organometallic precursor. Both a capacity and reversibility improvement were achieved with respect to Pure TiO$_2$ sample through this fast and facile synthesis, even though the results did not outperform HT1 sample, as shown in Fig. 6.

By simple milling the conductive carbon, a good enhancement of the specific capacity is observed, and even though slow rates capacity is lower than HT1, at high current densities an improvement of the milled sample is highlighted. This could be explained by the good dispersion of the carbon material due to the high energy milling, that can cause the reduction of the lateral size of the graphene platelets, thus obtaining a more distributed graphene network, as proven by HR-TEM. HT1, showed better results at all C rates other than 30 C whilst having the same carbon loading, probably because of the high anatase content, which is a material that has better electrochemical performances respect to TiO$_2$ (II).

3.5. SPXRD

SXRPD patterns were collected operando both for the Pure TiO$_2$ electrode and for the most performing 99:1 systems HT1 and BM upon cycling at C/10. From a structural point of view, the data acquired show a smooth phase transition of the anatase upon lithiation. Fig. 7 reports the data collected on the Pure TiO$_2$ electrode. For the sake of clarity, the minor fraction of brookite (barely observed at this grade of profile resolution) was neglected from the following analysis. The first complete discharge (about first 10 h in Fig. 7) is followed by a complete charge (about from 10 to 20 h). During the first drop in voltage [region (a) in Fig. 7] the powder patterns can be entirely indexed using the anatase phase, the main reflections of which are indexed in the figure. In parallel to the establishment of the 1st plateau in the voltage [region (b)] the reduction in intensity of the tetragonal anatase peaks is accompanied by the increase of the Li$_x$TiO$_2$ orthorhombic peaks. Of particular relevance is the appearance of the 011, 004, 020, 121, and 114 peaks which are forbidden reflections in the $I4_1/amd$ lattice. During the 2nd plateau and across the switching in current of the 1st charge [region (c)] the entire electrode is lithiated to the orthorhombic phase. Upon reaching the minimum voltage, the Li$_x$TiO$_2$ phase shows further contraction along the c-axis and expansion along the a-axis, as highlighted by the shifting of the 004 and 200 reflections and as observed in detailed studies of pure TiO$_2$ nanoparticles [63], pointing to the formation of Li$_{0.5}$TiO$_2$, which corresponds to the maximum uptake of lithium. From the structural point of view, the 2nd plateau
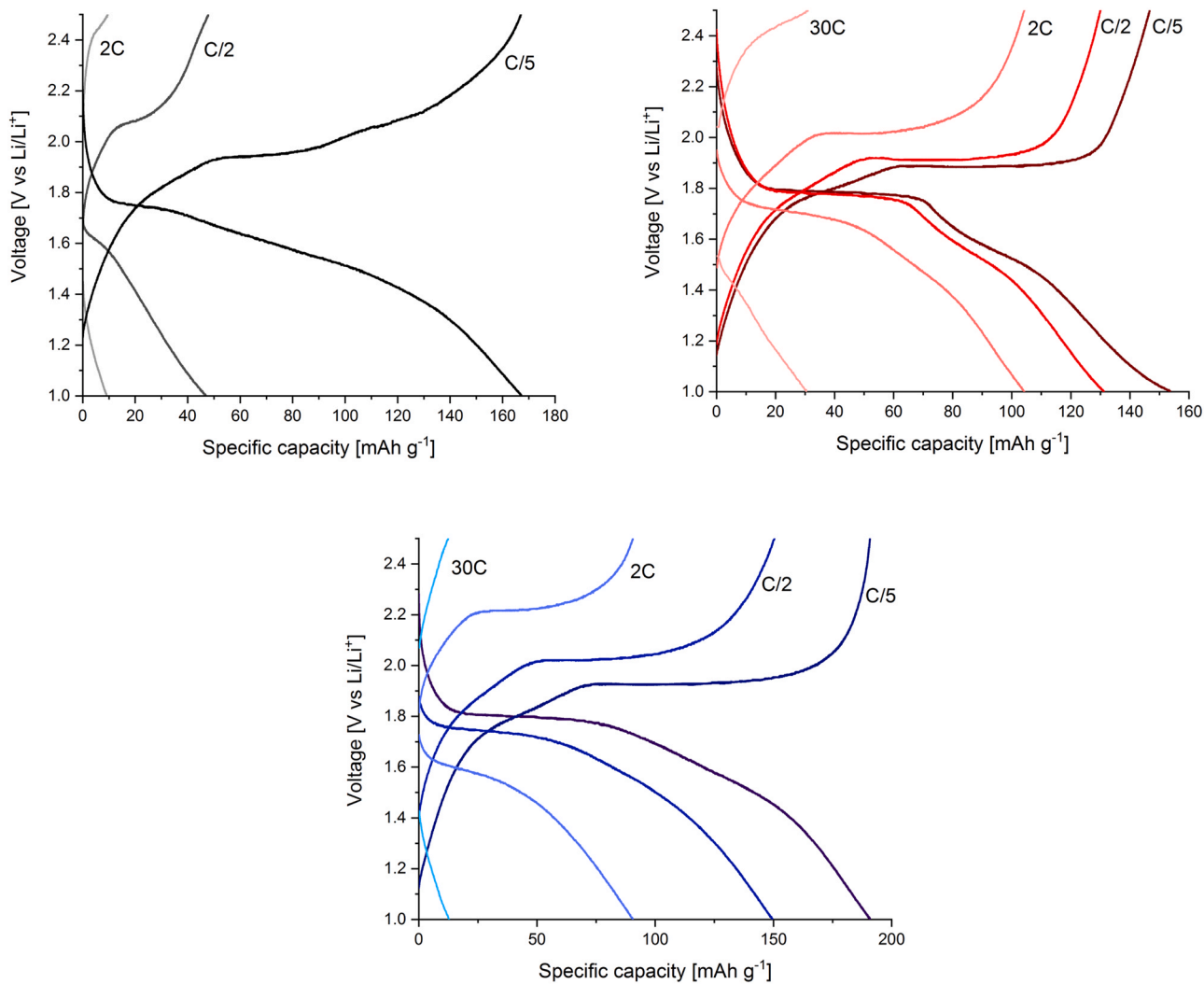
Fig. 5. Charge-discharge voltage profiles of Pure TiO$_2$, HT1 and HT2. Several C rates are shown to highlight the samples behavior at different conditions.
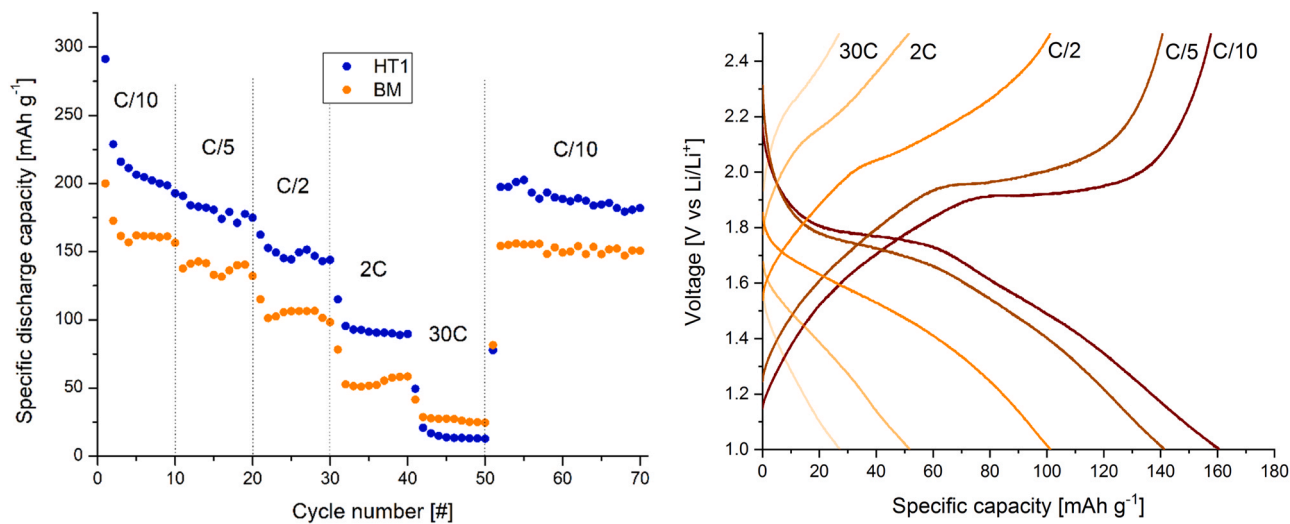

Fig. 6. GCD comparison between HT1 and BM (on the left). On the right, charge-discharge voltage profiles of BM at different C rates.
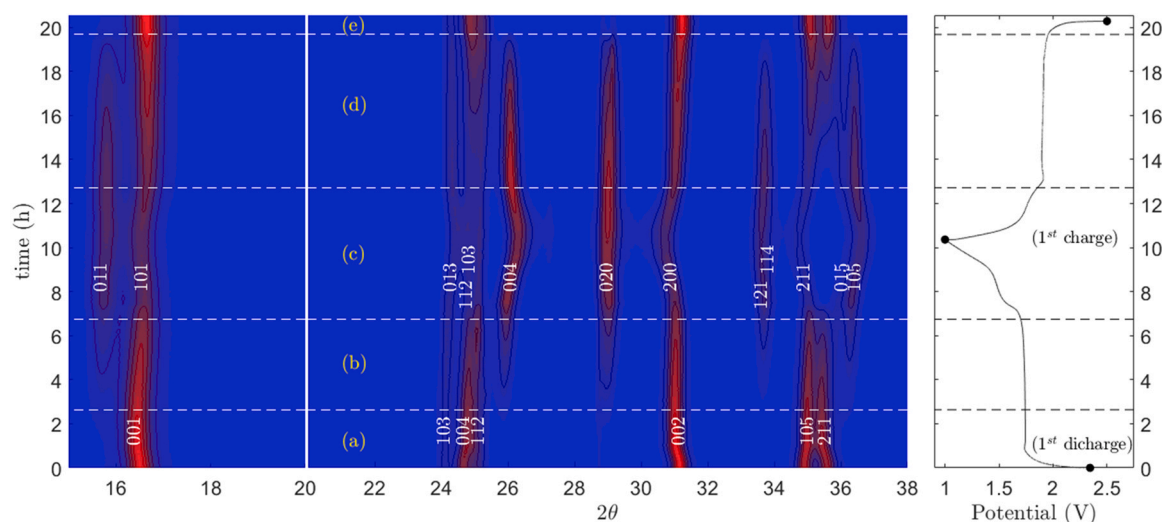
Fig. 7. 2D diffraction evolution (left panels) and galvanostatic discharge/charge profile (right panel) for the Pure TiO$_2$ half-cell cycled at C/10. Different indexing of peaks during time highlights the main reflections characterizing the evolution from the initial anatase structure to Li$_{0.5}$TiO$_2$ in the lithiated electrode. Dashed horizontal lines mark the topic onsets in the structure and discharge/charge profile (see main text). Contrast in the range 20–38° in 2θ has been increased compared to range 15–20° to show less intense peaks.

during the charge process [region (d)] and the final rise in voltage [region (e)] display specular features with respect to the discharge process, ultimately leading to the complete and reversible conversion of Li$_{0.5}$TiO$_2$ to anatase.

The diffraction patterns of the electrodes composed by HT1 and BM samples (Figs. 8 and 9) appear much less clear in terms of peaks separation and intensity compared to Pure TiO$_2$ and the main cause might be found behind factors such as a lower fraction of active material under the beam, finer sizes of the particles, and an increased disorder. For example, in both Figs. 8 and 9, the 105 and 211 reflections in the anatase phase or the 011 and 101 ones in the Li$_x$TiO$_2$ phase, which were well deconvoluted in the Pure TiO$_2$ patterns, now appear as single convoluted peaks for HT1 and BM, due to profile broadening. Moreover, an increased number of extrinsic

features was observed in these patterns (mostly due to scattering from the aluminum electrodes) which were not possible to mask completely during the data reduction procedure or fit as background during the refinement process. Given the scarce resolution, a quantitative analysis based on the Rietveld approach appears daunting. Nonetheless, it is still possible to qualitatively follow the structural changes occurring during the discharge/charge process by focusing the attention on the most relevant ranges highlighting changes in symmetry and appearance of forbidden reflections. For this purpose, Figs. 8 and 9 display magnified ranges at 2θ= 15–18° and 30–38°, less affected by extrinsic features and featuring the main distinct peaks of anatase and Li$_x$TiO$_2$. The HT1 electrode displays a progressive lowering in intensity of the 001, 002, 105, and 211 reflections during the beginning of the first discharge [region (a) in
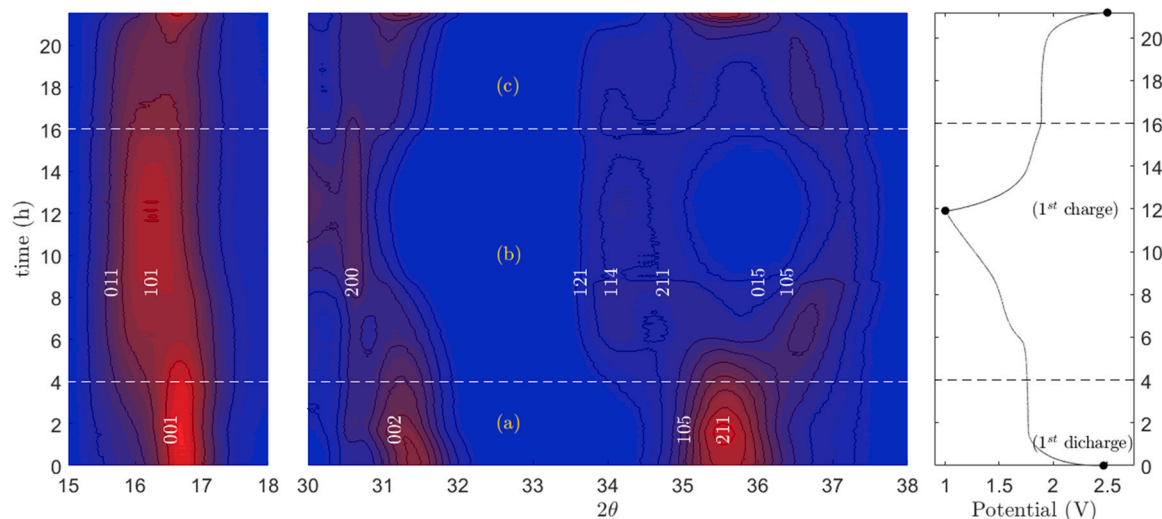

Fig. 8. 2D diffraction evolution (left panels) and galvanostatic discharge/charge profile (right panel) for the HT1 half-cell cycled at C/10. Different indexing of peaks during time highlights the main reflections characterizing the evolution from the initial anatase structure to Li$_x$TiO$_2$ in the lithiated electrode. Dashed horizontal lines mark the topic onsets in the structure and discharge/charge profile (see main text). Contrast in the range 30–38° in 2θ has been increased compared to range 15–18° to show less intense peaks.
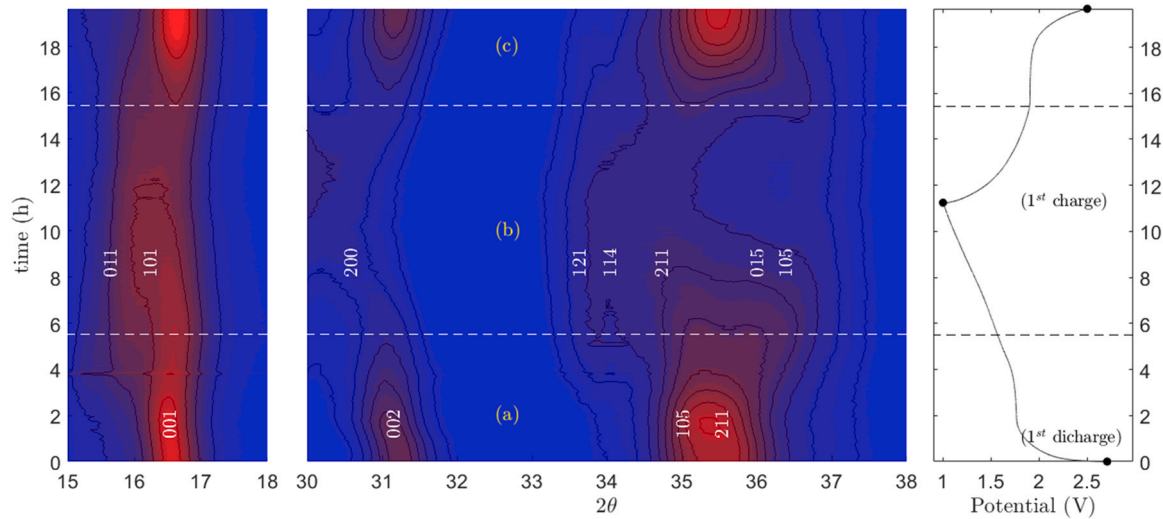
Fig. 9. 2D diffraction evolution (left panels) and galvanostatic discharge/charge profile (right panel) for the BM half-cell cycled at C/10. Different indexing of peaks during time highlights the main reflections characterizing the evolution from the initial anatase structure to Li$_x$TiO$_2$ in the lithiated electrode. Dashed horizontal lines mark the topic onsets in the structure and discharge/charge profile (see main text). Contrast in the range 30–38° in 2θ has been increased compared to range 15–18° to show less intense peaks.
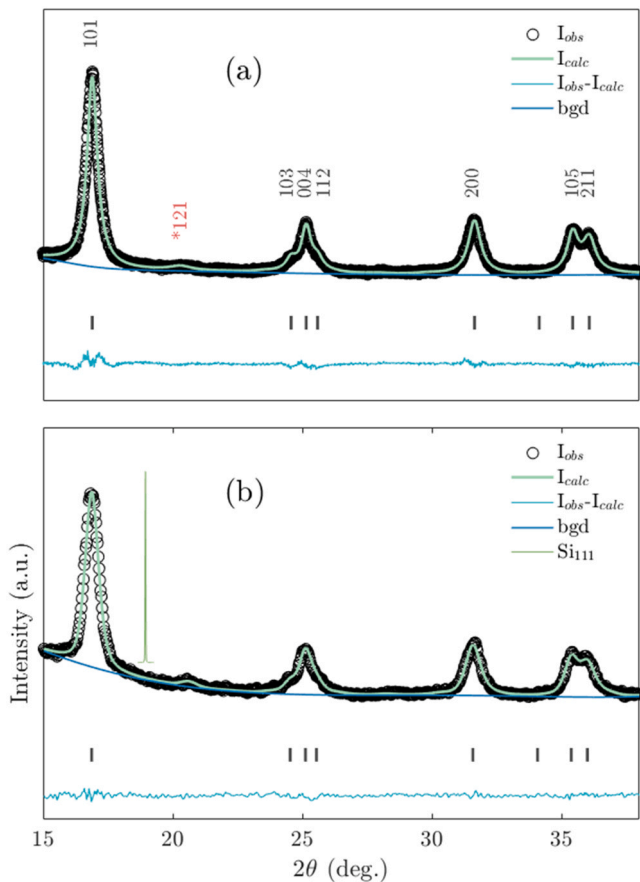

Fig. 10. Room temperature synchrotron X-ray powder diffraction data and Rietveld refinements for (a) Pure TiO$_2$ and (b) HT1 powders. Vertical tick marks highlight reflections of anatase, with Miller's indexes in (a) featuring the main reflections of anatase (black). The most detectable reflection of brookite (121) is emphasized (in red) by an asterisk. The silicon 111 reflection is also displayed, rescaled in intensity, in (b) to show the instrumental resolution.

Fig. 8] followed by the appearance of orthorhombic features (in particular, reflections 011 and 101 at low angle and 200, 114, and 105 at higher angles) during the second part of the discharge and the beginning of the 1st charge [region (b)]. At the maximum extent of lithiation the peaks ascribed to the anatase phase are completely extinct. In the final part of the 2nd discharge [region (c)] the anatase peaks appear again at the expenses of the Li$_x$TiO$_2$ features.

The discharge/charge process of the BM electrode (Fig. 9) is even harder to quantify due to a lack of distinct features in the high angle range. However, it is still possible to trace the transition from anatase to Li$_x$TiO$_2$ by following the initial shift of the 001 peak [region (a) in Fig. 9] followed by its further broadening, marking the appearance of the 011 and 101 Li$_x$TiO$_2$ reflections [region (b)] and the ultimate reversible conversion to anatase in the second half of the 1st charge process [region (c)], marked by the reappearance of the 002, 105, and 211 reflections of anatase. While the 1st plateau at 1.7 V, corresponding to the first transition from anatase to Li$_x$TiO$_2$ (for x between 0.05 and 0.25) is clearly observed in all three samples, the second plateau, related to the further lithiation from $x = 0.25$–0.5, is clearly discernible only for Pure TiO$_2$ and HT1, suggesting a less-uniform trend of lithiation in BM. Overall, the best performance obtained for HT1 calls for a more detailed comparison between pristine TiO$_2$ and the sample obtained via hydrothermal impregnation. Fig. 10 reports the high-resolution SXRPD patterns of Pure TiO$_2$ and HT1 as measured for the powders using the 1D detector and the goniometer, showing the same range displayed in Fig. 7.

The best refinement was obtained using both anatase and brookite phases and allows for the profile fitting employing the model for uniaxial size broadening and the isotropic microstrain approximation. The results are displayed in Table 3. The sample obtained via hydrothermal method using only 1 wt% of TEGO results in a slightly larger fraction of anatase composed by smaller nanoparticles (below 10 nm as opposed to 15–20 nm of Pure TiO$_2$). A slight variation is also observed in the refinement of the lattice parameters, which leads to a slightly expanded lattice for HT1. Microstrain effects appear to be not negligible and comparable for both

Table 3

Rietveld refined parameters for Pure TiO_2 and HT1 analysed from high-resolution SXRPD reporting the relative weight fractions for anatase and Brookite and main structural parameters for anatase (axial and equatorial domain sizes, isotropic microstrain, and lattice parameters).

	Anatase (%)	size-ax (nm)	size-eq (nm)	μ-strain (Δd/d %)	Brookite (%)	size-iso (nm)	a,b (Å)	c (Å)	R_{wp} (%)
Pure TiO_2	87.1(3)	19.3(4)	14.7(2)	0.85(4)	12.9(6)	6.0(3)	3.7911(4)	9.4972(7)	6.7
HT1	91.5(5)	11.6(4)	9.25(16)	0.93(1)	8.5(1.0)	7.2(2)	3.7977(4)	9.5086(12)	4.4

samples, most likely due to surface effects typical of nanosized particles.

The reduced size of crystalline domains for HT1 is suggestive of a more efficient nucleation process occurring when TEGO is used as support.

4. Conclusion

A novel active material for negative electrodes in LIBs consisting in TiO_2 nanoparticles decorated defective graphene has been investigated. Two facile, green and scalable synthetic routes have been developed to obtain TiO_2 graphene nanocomposites, both of them employing thermal exfoliated graphene oxide as a carbon scaffold. On the one hand, the presence of graphene allowed to improve the electron transport in the composite, overcoming the known poor electrical conductivity of titanates. On the other, the strong interaction between TiO_2 nanoparticles and graphene defects, which behave as nucleation catalyst during the synthetic step, appeared effective both to control the TiO_2 nanoparticle dimensions and to favour the formation of the most electroactive anatase polymorph, as compared to brookite and rutile. Moreover, the small dimensions of anatase nanoparticles, down to 10 nm, allowed to improve the Li insertion inside the TiO_2 crystals and to obtain high rates capacity even at stressful current densities in tested electrodes.

These results are clearly impactful from an industrial perspective; in fact, recently, lithium-titanium dioxide batteries have aroused growing interest, due to their performance at very high charge/discharge rates and for their superior stability upon cycling, with respect to current Li-ion technology. For these reasons, several companies have also started working and marketing TiO_2 based batteries. In this context, the herein proposed synthetic process can be an interesting candidate as a scalable and performing method for the production of LIBs electrodes. The overall best sample was the 99:1 TiO_2:TEGO w/w, which achieved a stable 180 mA h/g capacity at C/10 rate after prolonged cycling. The reversibility and stability of the device was also investigated, by means of operando synchrotron light diffraction, which evidenced a fully symmetrical (thus reversible) evolution of the crystal phase between the lithiation (discharge) and delithiation (charge) of the electrode for all the materials tested.

CRediT authorship contribution statement

Michele Sidoli: Conceptualization, Data curation, Formal analysis, Investigation, Methodology, Validation, Visualization, Writing – original draft, Writing – review & editing. **Giacomo Magnani:** Investigation, Methodology, Resources, Supervision, Writing – original draft, Writing – review & editing. **Laura Fornasini:** Investigation, Methodology, Resources, Writing – original draft. **Silvio Scaravonati:** Investigation, Methodology, Resources. **Alberto Morenghi:** Investigation, Methodology, Resources. **Vincenzo Vezzoni:** Data curation, Formal analysis, Investigation, Validation, Visualization. **Danilo Bersani:** Supervision, Validation, Visualization. **Giovanni Bertoni:** Data curation, Formal analysis, Investigation, Validation, Visualization, Writing – original draft. **Mattia Gaboardi:** Data curation, Formal analysis, Investigation, Validation, Visualization, Writing – original draft. **Mauro Riccò:** Conceptualization, Methodology, Project administration, Resources, Supervision, Validation, Writing – review & editing. **Daniele Pontiroli:** Conceptualization, Funding acquisition, Methodology, Project administration, Resources, Supervision, Validation, Visualization, Writing – original draft, Writing – review & editing.

Data Availability

Data will be made available on request.

Declaration of Competing Interest

The authors declare that they have no known competing financial interests or personal relationships that could have appeared to influence the work reported in this paper.

Acknowledgements

References

[1] M.S. Whittingham, R.F. Savinell, T. Zawodzinski, Introduction: batteries and fuel cells, Chem. Rev. 104 (2004) 4243–4244, https://doi.org/10.1021/CR020705E

[2] A. Eddahech, O. Briat, J.M. Vinassa, Performance comparison of four lithium–ion battery technologies under calendar aging, Energy 84 (2015) 542–550, https://doi.org/10.1016/J.ENERGY.2015.03.019

[3] Y.N. Singhbabu, P.N. Didwal, K. Jang, J. Jang, C.J. Park, M.H. Ham, Green synthesis of a reduced-graphene-oxide wrapped nickel oxide nano-composite as an anode for high-performance lithium-ion batteries, ChemistrySelect 7 (2022) e202200676, https://doi.org/10.1002/SLCT.202200676

[4] Y. Chen, H. Chen, F.H. Du, X. Shen, Z. Ji, H. Zhou, A. Yuan, In-situ construction of nano-sized Ni-NiO-MoO2 heterostructures on holey reduced graphene oxide nanosheets as high-capacity lithium-ion battery anodes, J. Alloy. Compd. 926 (2022) 166847, https://doi.org/10.1016/J.JALLCOM.2022.166847

[5] Y. Li, S. Wang, Y.B. He, L. Tang, Y.V. Kaneti, W. Lv, Z. Lin, B. Li, Q.H. Yang, F. Kang, Li-ion and Na-ion transportation and storage properties in various sized TiO 2 spheres with hierarchical pores and high tap density, J. Mater. Chem. A Mater. 5 (2017) 4359–4367, https://doi.org/10.1039/C6TA08611J

[6] Y. Wang, J. Li, X. Li, H. Jin, W. Ali, Z. Song, S. Ding, Metal–organic-framework derived Co@CN modified horizontally aligned graphene oxide array as free-standing anode for lithium-ion batteries, J. Mater. Chem. A Mater. 10 (2022) 699–706, https://doi.org/10.1039/D1TA07638H

[7] N. Takami, H. Inagaki, Y. Tatebayashi, H. Saruwatari, K. Honda, S. Egusa, High-power and long-life lithium-ion batteries using lithium titanium oxide anode for automotive and stationary power applications, J. Power Sources 244 (2013) 469–475, https://doi.org/10.1016/J.JPOWSOUR.2012.11.055

[8] M. Fehse, E. Ventosa, Is TiO2(B) the future of titanium-based battery materials, Chempluschem 80 (2015) 785–795, https://doi.org/10.1002/CPLU.201500038

[9] Y.-S. Hu, L. Kienle, Y.-G. Guo, J. Maier, High lithium electroactivity of nanometer-sized rutile TiO2, Adv. Mater. 18 (2006) 1421–1426, https://doi.org/10.1002/adma.200502723

[10] X. Yang, Y. Yang, H. Hou, Y. Zhang, L. Fang, J. Chen, X. Ji, Size-tunable single-crystalline anatase TiO2 cubes as anode materials for lithium ion batteries, J. Phys. Chem. C (2015), https://doi.org/10.1021/jp512289g

[11] E. Ventosa, E. Madej, G. Zampardi, B. Mei, P. Weide, H. Antoni, F. La Mantia, M. Muhler, W. Schuhmann, Solid electrolyte interphase (SEI) at TiO2 electrodes

in Li-ion batteries: defining apparent and effective SEI based on evidence from x-ray photoemission spectroscopy and scanning electrochemical microscopy, ACS Appl. Mater. Interfaces 9 (2017) 3123–3130, https://doi.org/10.1021/ACSAMI.6B13306

[12] S.J. Park, H. Kim, Y.J. Kim, H. Lee, Preparation of carbon-coated TiO2 nanostructures for lithium-ion batteries, Electrochim. Acta 56 (2011) 5355–5362, https://doi.org/10.1016/j.electacta.2011.03.119

[13] X. Xin, X. Zhou, J. Wu, X. Yao, Z. Liu, Scalable synthesis of TiO2/graphene nanostructured composite with high-rate performance for lithium ion batteries, ACS Nano (2012), https://doi.org/10.1021/nn304725m

[14] N. Li, G. Liu, C. Zhen, F. Li, L. Zhang, H.M. Cheng, Battery performance and photocatalytic activity of mesoporous anatase TiO2 nanospheres/graphene composites by template-free self-assembly, Adv. Funct. Mater. 21 (2011) 1717–1722, https://doi.org/10.1002/ADFM.201002295

[15] S. Hoon Nam, H.-S. Shim, Y.-S. Kim, M. Ahmad Dar, J. Guk Kim, W. Bae Kim, Ag or Au nanoparticle-embedded one-dimensional composite TiO2 nanofibers prepared via electrospinning for use in lithium-ion batteries, ACS Appl. Mater. Interfaces 2 (2010) 2046–2052, https://doi.org/10.1021/am100319u

[16] B. Erjavec, R. Dominko, P. Umek, S. Sturm, S. Pejovnik, M. Gaberscek, J. Jamnik, RuO2-wired high-rate nanoparticulate TiO2 (anatase): Suppression of particle growth using silica, Electrochem Commun. 10 (2008) 926–929, https://doi.org/10.1016/J.ELECOM.2008.04.006

[17] S. Yoon, B.H. Ka, C. Lee, M. Park, S.M. Oh, Preparation of nanotube TiO2-carbon composite and its anode performance in lithium-ion batteries, Electrochem. Solid-State Lett. 12 (2008) A28, https://doi.org/10.1149/1.3035981

[18] L. Zuniga, V. Agubra, D. Flores, H. Campos, J. Villareal, M. Alcoutlabi, Multichannel hollow structure for improved electrochemical performance of TiO2/Carbon composite nanofibers as anodes for lithium ion batteries, J. Alloy. Compd. 686 (2016) 733–743, https://doi.org/10.1016/J.JALLCOM.2016.06.089

[19] R. Wu, S. Shen, G. Xia, F. Zhu, C. Lastoskie, J. Zhang, Soft-templated self-assembly of mesoporous anatase TiO2/carbon composite nanospheres for high-performance lithium ion batteries, ACS Appl. Mater. Interfaces 8 (2016) 19968–19978, https://doi.org/10.1021/ACSAMI.6B03733

[20] D. Pontiroli, S. Scaravonati, M. Sidoli, G. Magnani, L. Fornasini, C. Milanese, M. Riccò, Fullerene mixtures as negative electrodes in innovative Na-ion batteries, Chem. Phys. Lett. 731 (2019) 136607, https://doi.org/10.1016/J.CPLETT.2019.136607

[21] L. Fornasini, S. Scaravonati, G. Magnani, A. Morenghi, M. Sidoli, D. Bersani, G. Bertoni, L. Aversa, R. Verucchi, M. Riccò, P.P. Lottici, D. Pontiroli, In situ decoration of laser-scribed graphene with TiO2 nanoparticles for scalable high-performance micro-supercapacitors, Carbon N. Y. 176 (2021) 296–306, https://doi.org/10.1016/J.CARBON.2021.01.129

[22] A. Morenghi, S. Scaravonati, G. Magnani, M. Sidoli, L. Aversa, R. Verucchi, G. Bertoni, M. Riccò, D. Pontiroli, Asymmetric supercapacitors based on nickel decorated graphene and porous graphene electrodes, Electrochim. Acta 424 (2022) 140626, https://doi.org/10.1016/J.ELECTACTA.2022.140626

[23] F. Liu, X. Sun, Y. Liu, X. Song, J. Gao, G. Qin, TiO2 nanorods confined in porous V2O5 nanobelts and interconnected carbon channels for sodium ion batteries, Appl. Surf. Sci. 473 (2019) 873–884, https://doi.org/10.1016/J.APSUSC.2018.12.026

[24] D. Wang, D. Choi, J. Li, Z. Yang, Z. Nie, R. Kou, D. Hu, C. Wang, L.V. Saraf, J. Zhang, I.A. Aksay, J. Liu, Self-assembled TiO 2-graphene hybrid nanostructures for enhanced Li-ion insertion, ACS Nano 3 (2009) 907–914, https://doi.org/10.1021/nn900150y

[25] X. Yu, D. Lin, P. Li, Z. Su, Recent advances in the synthesis and energy applications of TiO2-graphene nanohybrids, Sol. Energy Mater. Sol. Cells 172 (2017) 252–269, https://doi.org/10.1016/J.SOLMAT.2017.07.045

[26] D. Cai, P. Lian, X. Zhu, S. Liang, W. Yang, H. Wang, High specific capacity of TiO2-graphene nanocomposite as an anode material for lithium-ion batteries in an enlarged potential window, Electro Acta 74 (2012) 65–72, https://doi.org/10.1016/J.ELECTACTA.2012.03.170

[27] M. Wagemaker, W.J.H. Borghols, E.R.H. Van Eck, A.P.M. Kentgens, G.J. Kearley, F.M. Mulder, The influence of size on phase morphology and Li-ion mobility in nanosized lithiated anatase TiO2, Chem. - A Eur. J. 13 (2007) 2023–2028, https://doi.org/10.1002/chem.200600803

[28] M. Wagemaker, W.J.H. Borghols, F.M. Mulder, Large impact of particle size on insertion reactions. A case for anatase LixTiO2, J. Am. Chem. Soc. 129 (2007) 4323–4327, https://doi.org/10.1021/ja067733p

[29] W. Li, F. Wang, S. Feng, J. Wang, Z. Sun, B. Li, Y. Li, J. Yang, A.A. Elzatahry, Y. Xia, D. Zhao, Sol-gel design strategy for ultradispersed tio2 nanoparticles on graphene for high-performance lithium ion batteries, J. Am. Chem. Soc. 135 (2013) 18300–18303, https://doi.org/10.1021/JA4100723/SUPPL_FILE/JA4100723_SI_001.PDF

[30] X. Xin, X. Zhou, J. Wu, X. Yao, Z. Liu, Scalable synthesis of TiO2/graphene nanostructured composite with high-rate performance for lithium ion batteries, ACS Nano 6 (2012) 11035–11043, https://doi.org/10.1021/NN304725M/SUPPL_FILE/NN304725M_SI_001.PDF

[31] S. Yang, X. Feng, K. Müllen, Sandwich-like, graphene-based titania nanosheets with high surface area for fast lithium storage, Adv. Mater. 23 (2011) 3575–3579, https://doi.org/10.1002/ADMA.201101599

[32] H. Cao, B. Li, J. Zhang, F. Lian, X. Kong, M. Qu, Synthesis and superior anode performance of TiO2@reduced graphene oxide nanocomposites for lithium ion batteries, J. Mater. Chem. 22 (2012) 9759–9766, https://doi.org/10.1039/C2JM00007E

[33] L. Shen, X. Zhang, H. Li, C. Yuan, G. Cao, Design and tailoring of a three-dimensional TiO 2-graphene-carbon nanotube nanocomposite for fast lithium storage,

[34] J. Liao, L. Shi, S. Yuan, Y. Zhao, J. Fang, Solvothermal synthesis of TiO2 nanocrystal colloids from peroxotitanate complex solution and their photocatalytic activities, J. Phys. Chem. C 113 (2009) 18778–18783, https://doi.org/10.1021/JP905720G

[35] C. Cavallari, S. Rols, H.E. Fischer, M. Brunelli, M. Gaboardi, G. Magnani, M. Riccò, D. Pontiroli, Neutron scattering study of nickel decorated thermally exfoliated graphite oxide, Int. J. Hydrogen Energy 44 (2019) 30999–31007, https://doi.org/10.1016/J.IJHYDENE.2019.09.226

[36] J.C. Pramudita, D. Pontiroli, G. Magnani, M. Gaboardi, C. Milanese, G. Bertoni, N. Sharma, M. Riccò, Effect of Ni-nanoparticles decoration on graphene to enable high capacity sodium-ion battery negative electrodes, Electrochim. Acta 250 (2017) 212–218, https://doi.org/10.1016/J.ELECTACTA.2017.08.049

[37] J.C. Pramudita, A. Rawal, M. Choucair, D. Pontiroli, G. Magnani, M. Gaboardi, M. Riccò, N. Sharma, Mechanisms of sodium insertion/extraction on the surface of defective graphenes, ACS Appl. Mater. Interfaces 9 (2016) 431–438, https://doi.org/10.1021/ACSAMI.6B13104

[38] C. Cavallari, D. Pontiroli, M. Jiménez-Ruiz, M. Johnson, M. Aramini, M. Gaboardi, S.F. Parker, M. Riccò, S. Rols, Hydrogen motions in defective graphene: the role of surface defects, Phys. Chem. Chem. Phys. 18 (2016) 24820–24824, https://doi.org/10.1039/C6CP04727K

[39] M. Gaboardi, R. Tatti, G. Bertoni, G. Magnani, R. Della Pergola, L. Aversa, R. Verucchi, D. Pontiroli, M. Riccò, Platinum carbonyl clusters decomposition on defective graphene surface, Surf. Sci. 691 (2020) 121499, https://doi.org/10.1016/j.susc.2019.121499

[40] J.C. Pramudita, D. Pontiroli, G. Magnani, M. Gaboardi, M. Riccò, C. Milanese, H.E.A.A. Brand, N. Sharma, Graphene and selected derivatives as negative electrodes in sodium- and lithium-ion batteries, ChemElectroChem 2 (2015) 600–610, https://doi.org/10.1002/celc.201402352

[41] M. Gaboardi, A. Bliersbach, G. Bertoni, M. Aramini, G. Vlahopoulou, D. Pontiroli, P. Mauron, G. Magnani, G. Salviati, A. Züttel, M. Riccò, Decoration of graphene with nickel nanoparticles: study of the interaction with hydrogen, J. Mater. Chem. A Mater. 2 (2014) 1039–1046, https://doi.org/10.1039/c3ta14127f

[42] C. Botas, P. Álvarez, P. Blanco, M. Granda, C. Blanco, R. Santamaría, L.J. Romasanta, R. Verdejo, M.A. López-Manchado, R. Menéndez, Graphene materials with different structures prepared from the same graphite by the Hummers and Brodie methods, Carbon N.Y. 65 (2013) 156–164, https://doi.org/10.1016/j.carbon.2013.08.009

[43] X. Zhao, W. Jin, J. Cai, J. Ye, Z. Li, Y. Ma, J. Xie, L. Qi, Shape- and size-controlled synthesis of uniform anatase TiO2 nanocuboids enclosed by active {100} and {001} facets, Adv. Funct. Mater. 21 (2011) 3554–3563, https://doi.org/10.1002/adfm.201100629

[44] C. Cavallari, D. Pontiroli, M. Jiménez-Ruiz, A. Ivanov, M. Mazzani, M. Gaboardi, M. Aramini, M. Brunelli, M. Riccò, S. Rols, Hydrogen on graphene investigated by inelastic neutron scattering, J. Phys. Conf. Ser. 554 (2014) 012009, https://doi.org/10.1088/1742-6596/554/1/012009

[45] S. Vantadori, G. Magnani, L. Mantovani, D. Pontiroli, C. Ronchei, D. Scorza, M. Sidoli, A. Zanichelli, M. Riccò, Effect of GO nanosheets on microstructure, mechanical and fracture properties of cement composites, Constr. Build. Mater. 361 (2022) 129368, https://doi.org/10.1016/J.CONBUILDMAT.2022.129368

[46] N. Li, G. Liu, C. Zhen, F. Li, L. Zhang, H.M. Cheng, Battery performance and photocatalytic activity of mesoporous anatase TiO2 nanospheres/graphene composites by template-free self-assembly, Adv. Funct. Mater. 21 (2011) 1717–1722, https://doi.org/10.1002/ADFM.201002295

[47] R. Mo, Z. Lei, K. Sun, D. Rooney, R.W. Mo, Z.Y. Lei, K.N. Sun, D. Rooney, Facile synthesis of anatase TiO2 quantum-dot/graphene-nanosheet composites with enhanced electrochemical performance for lithium-ion batteries, Adv. Mater. 26 (2014) 2084–2088, https://doi.org/10.1002/ADMA.201304338

[48] S. Scaravonati, M. Sidoli, G. Magnani, A. Morenghi, M. Canova, J.-H. Kim, M. Riccò, D. Pontiroli, Combined capacitive and electrochemical charge storage mechanism in high performance graphene-based lithium-ion batteries, Mater Today Energy (2021) 100928, https://doi.org/10.1016/J.MTENER.2021.100928

[49] L. Rebuffi, J.R. Plaisier, M. Abdellatief, A. Lausi, A.P. Scardi, Mcx: a synchrotron radiation beamline for X-ray diffraction line profile analysis, Z. Anorg. Allg. Chem. 640 (2014) 3100–3106, https://doi.org/10.1002/zaac.201400163

[50] S.W. Freiman, Standard Reference Material ® 660a Lanthanum Hexaboride Powder Line Position and Line Shape Standard for Powder Diffraction Standard Reference Materials Program, 2000.

[51] B.H. Toby, R.B.Von Dreele, GSAS-II: the genesis of a modern open-source all purpose crystallography software package, J. Appl. Crystallogr 46 (2013) 544–549, https://doi.org/10.1107/S0021889813003531

[52] S.R. Material, Silicon Powder (Line Position and Line Shape Standard for Powder Diffraction), 2015, pp. 1–5.

[53] H. Zhang, J.F. Banfield, Thermodynamic analysis of phase stability of nanocrystalline titania, J. Mater. Chem. 8 (1998) 2073–2076, https://doi.org/10.1039/A802619J

[54] D. Bersani, P.P. Lottici, X.Z. Ding, Phonon confinement effects in the Raman scattering by TiO2 nanocrystals, Appl. Phys. Lett. 72 (1998) 73–75, https://doi.org/10.1063/1.120648

[55] A. Gajovi, M. Stubičar, M. Ivanda, K. Furi, Raman spectroscopy of ball-milled TiO2, J. Mol. Struct. 563–564 (2001) 315–320, https://doi.org/10.1016/S0022-2860(00)00790-0

[56] A. Gajović, M. Stubičar, M. Ivanda, K. Furić, Raman spectroscopy of ball-milled TiO2, J. Mol. Struct. 563 (2001) 315–320, https://doi.org/10.1016/S0022-2860(00)00790-0

[57] A.C. Ferrari, Raman spectroscopy of graphene and graphite: disorder, electron–phonon coupling, doping and nonadiabatic effects, Solid State Commun. 143 (2007) 47–57, https://doi.org/10.1016/J.SSC.2007.03.052

[58] A.A. Belak, Y. Wang, A. Van der Ven, Kinetics of anatase electrodes: the role of ordering, anisotropy, and shape memory effects, Chem. Mater. 24 (2012) 2894–2898, https://doi.org/10.1021/CM300881T

[59] G. Wang, X. Shen, J. Yao, J. Park, Graphene nanosheets for enhanced lithium storage in lithium ion batteries, Carbon N.Y. 47 (2009) 2049–2053, https://doi.org/10.1016/J.CARBON.2009.03.053

[60] A.L.M. Reddy, A. Srivastava, S.R. Gowda, H. Gullapalli, M. Dubey, P.M. Ajayan, Synthesis of nitrogen-doped graphene films for lithium battery application, ACS Nano 4 (2010) 6337–6342, https://doi.org/10.1021/NN101926G/SUPPL_FILE/NN101926G_SI_001.PDF

[61] H. Kim, Y. Son, C. Park, J. Cho, H.C. Choi, Catalyst-free direct growth of a single to a few layers of graphene on a germanium nanowire for the anode material of a lithium battery, Angew. Chem. 125 (2013) 6113–6117, https://doi.org/10.1002/ANGE.201300896

[62] J.-Y.Y. Shin, D. Samuelis, J. Maier, Sustained lithium-storage performance of hierarchical, nanoporous anatase TiO2 at high rates: emphasis on interfacial storage phenomena, Adv. Funct. Mater. 21 (2011) 3464–3472, https://doi.org/10.1002/adfm.201002527

[63] H. Liu, C.P. Grey, Influence of particle size, cycling rate and temperature on the lithiation process of anatase TiO2, J. Mater. Chem. A Mater. 4 (2016) 6433–6446, https://doi.org/10.1039/C6TA00673F